Mixing processes in the vitreous chamber induced by eye rotations

Mixing processes in the vitreous chamber induced by eye rotations

Alessandro Stocchino[1], Rodolfo Repetto[2] and Jennifer H Siggers[3]

[1] Department of Civil, Environmental and Architectural Engineering, University of Genoa, Italy
[2] Department of Engineering of Structures, Water and Soil, University of L'Aquila, Italy
[3] Department of Bioengineering, Imperial College London, London SW7 2AZ, UK

E-mail: jorma@diam.unige.it

Abstract

In this paper, we study a model of flow in the vitreous humour in the posterior chamber of the human eye, induced by saccadic eye rotations. We concentrate on the effect of the shape of the chamber upon the mixing properties of the induced flows. We make particle image velocimetry measurements of the fluid velocity in a transparent plastic (Perspex) model of the posterior chamber during sinusoidal torsional oscillations about a vertical axis. We use a Newtonian fluid to model the vitreous humour, which is most realistic when either the vitreous humour is liquefied or has been replaced by purely viscous tamponade fluids. The model of the posterior chamber is a sphere with an indentation, representing the effect of the lens. In spite of the purely periodic forcing, a steady streaming flow is generated, which plays a fundamental role in the mixing processes in the domain. The streaming flow differs markedly from that in a perfect sphere, and its topological characteristics change substantially as the frequency of oscillation varies. We discuss the flow characteristics in detail and show that, for physiological parameter values, the Péclet number (based on a suitable measure of the steady streaming velocity) is large, suggesting that advection strongly dominates over diffusion for mass transport phenomena. We also compute particle trajectories based on the streaming velocity and use these to investigate the stirring properties of the flow.

1. Introduction

The vitreous humour occupies the posterior chamber of the eye, which is a roughly spherical space that accounts for the majority of the volume of the eye. The vitreous humour maintains the shape of the eye, promotes adherence between the retina and the choroid and acts as a barrier between the anterior and posterior segments of the eye. Dynamical motion of the

vitreous humour can be induced by movements of the eyeball, and the shear stress at the retina induced by this motion may be linked to the incidence of rhegmatogeneous retinal detachment (David *et al* 1998).

Another important application of vitreous humour dynamics is their effect on mass transport in the posterior chamber. Some eye conditions (age-related macular degeneration, glaucoma, diabetic retinopathy) are treated by intravitreal delivery of drugs through implants and direct injections into the vitreous cavity (Yasukawa *et al* 2004) or via the transscleral pathway (Balachandran and Barocas 2008). This enables significantly higher drug concentrations to reach the retina than is possible with topical or systemic administration. Many drugs have a narrow range of concentrations over which they are effective, meaning that an understanding of mass transport in the vitreous humour is vital. Diffusive transport in the vitreous humour has been extensively studied using theoretical and numerical models (see Ethier *et al* (2004) for a comprehensive bibliography), and a few *in vivo* studies have also been performed (e.g. Atluri and Mitra (2003) and Cunha-Vaz (2004)). Advection due to flow in the vitreous cavity can also play a very important role. There is a slow flow across the eye from the hyaloid membrane (anterior) to the retina (posterior) driven by a small pressure gradient (studied in Balachandran and Barocas (2008), Kathawate and Acharya (2008) and Xu *et al* (2000)), and also a flow induced by eye rotations. In some people, the fluid in the posterior chamber is approximately Newtonian, which may occur as a result of liquefaction of the vitreous humour due to synchysis (degradation of the collagenous framework), or after a vitrectomy (replacement of the vitreous humour by tamponade fluids), and for these patients Repetto *et al* (2009) estimated that vitreous motion due to eye rotations is much more important in inducing drug transport than diffusive processes.

A detailed understanding of vitreous motion induced by eye rotations is a prerequisite to a study of the drug transport in the vitreous cavity. David *et al* (1998) developed an analytical model to determine the flow of vitreous humour due to eye rotations. They modelled the vitreous humour as a viscoelastic material with the characteristics measured in Lee *et al* (1992). The vitreous chamber was assumed to be a sphere performing small-amplitude harmonic torsional oscillations about an axis passing through its centre, and the authors calculated the velocity profiles that are generated.

Repetto *et al* (2005) used a spherical, Perspex, magnified-scale model of the vitreous chamber filled with a Newtonian fluid. The model was placed on a motor, which performed prescribed torsional oscillations that were either sinusoidal or were based on measurements of real eye movements, and particle image velocimetry (PIV) measurements of fluid motion were taken during the experiment. A similar experimental technique, together with a theoretical model, was used in Repetto *et al* (2008) to show that the flow has a streaming component in addition to the leading-order oscillatory component, consisting of two counter-rotating toroidal vortices, one in each hemisphere. In reality, the vitreous chamber is not perfectly spherical, as, typically, the antero-posterior axis is slightly shorter than the other two axes and, in the anterior part of the chamber an indentation is present, caused by the lens. Moreover, symmetry in the nasal/temporal direction might be broken by the presence of the optic disc. The largest departure from the spherical shape is, however, due to the presence of the lens, which induces a change of curvature of the inner surface of the vitreous chamber. Stocchino *et al* (2007) studied the effect of the non-sphericity experimentally, using a spherical domain with an indentation representing the lens. The axis of rotation and the line joining the centre of the indentation and the centre of the circle were at 90° to one another. They measured the characteristics of the flow field, and one of their main findings is that a circulation is generated every half period behind the indentation, which proceeds to migrate towards the centre of the domain, where it is annihilated. Balachandran *et al* (2008) investigated vitreous motion
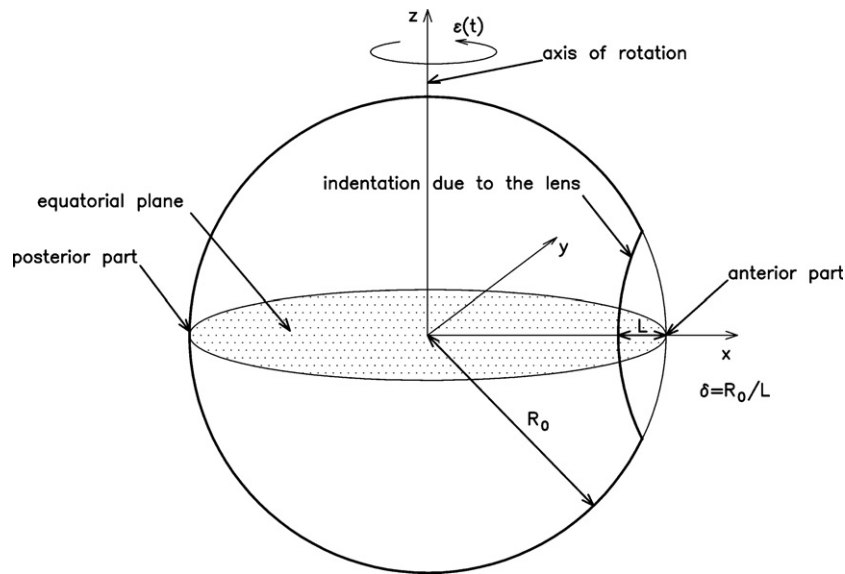
Figure 1. Sketch of the geometry under consideration.

induced by eye rotations numerically, and their findings are in qualitative agreement with the experimental results mentioned in Stocchino *et al* (2007). Repetto *et al* (2009) studied this system analytically and found the streaming flow generated in the non-spherical domain. The most striking feature of this flow is the presence of two counter-rotating steady circulations centred on the equatorial plane (which is the plane of symmetry perpendicular to the rotation axis that contains the centre of the indentation).

In this paper, we adopt an experimental approach and consider sinusoidal torsional oscillations of a model of the posterior chamber. The flow separates into an oscillatory component and a steady streaming component. The steady component of the flow is expected to have a much greater influence on the stirring properties of the flow (Repetto *et al* 2009) than the oscillatory component, and so in this paper we consider only the steady component. We find the Péclet number associated with the flow to be very large, and hence diffusion plays a minor role in mass transport. We describe the topological characteristics of the flow in detail and use a variety of techniques to estimate their mixing properties.

2. Material and methods

2.1. Experimental procedure

In this study, we employed, with suitable modifications, the apparatus described in detail in Repetto *et al* (2005) and Stocchino *et al* (2007), and here we briefly recall the main characteristics. We model the vitreous chamber using a Perspex container with an internal cavity. The shape of the cavity is obtained from the smoothed intersection of two spheres of equal radius $R_0 = 40.8$ mm (figure 1). We used this shape in order to isolate and investigate the effect of the indentation due to the lens alone, which is the most important in modifying flow field characteristics with respect to the spherical case. This choice also allows for direct comparison with previous experiments (Stocchino *et al* 2007) and analytical predictions

(Repetto *et al* 2009). We thus neglect smaller geometrical effects, which we assume to have minor importance. This domain is approximately 3.7 times the typical size of the real posterior chamber. The geometry is characterized by the nondimensional parameter $\delta = L/R_0$, where L is the maximum depth of the indentation (figure 1). In real eyes, the lens shape changes to allow for adjustment of the focal distance, which leads to significant differences in vitreous chamber shape under different conditions. An analysis of a few real eye cross-sections from MRI scans performed by the authors suggests that δ may range approximately between 0.1 and 0.3. We therefore used three different models characterized by $\delta = 0.1$, 0.2 and 0.3. We also note that our vitreous chamber is rigid, i.e. we neglect the small deformation of the eye shape induced by the pulling action of the external muscles attached to the outside of the eye globe. This effect, however, is expected to be of minor importance for understanding fluid motion in the vitreous chamber.

The model was mounted on a computer-controlled motorized support that could reproduce any prescribed time-dependent torsional oscillation about the vertical diameter of the sphere. The plane orthogonal to the axis of rotation and containing the centres of the spheres is a plane of symmetry and is hereinafter referred to as 'the equatorial plane' (figure 1). We refer to the region near the indentation as 'anterior' and that far from the indentation as 'posterior'. In this study, we used periodic sinusoidal oscillations of angular position, characterized by angular frequency ω and amplitude ε. Real eye rotations may last for a few periods, but they are at best only approximately sinusoidal. However, we found in our experiments that, starting from rest, the flow becomes approximately periodic after a few periods, suggesting that our measurements are relevant even for relatively short intervals of approximately sinusoidal motion. Moreover, we will show that the flow field exhibits complex features, even in the relatively simple case of sinusoidal forcing, and understanding the flow field in more complex cases is not possible until we understand these. We leave the problem of non-sinusoidal oscillations for future work.

The cavity was filled with aqueous solutions of glycerol at concentrations between 70% and 98%. The dynamic viscosity of the fluid was measured at the beginning of each experimental run using a falling ball viscometer, and care was taken to maintain a constant room temperature during each experimental run so that the viscosity remained constant.

A 2D PIV system, synchronized with the torsional oscillations, was used to acquire two-dimensional velocity fields on a plane. In order to directly measure the steady streaming and filter out the oscillatory component of the flow, we set the pulse separation for image pairing to be a multiple of the oscillation period T. Since the equatorial plane is a plane of symmetry, the flow there has no vertical component, which means we can gain particular insight by inspecting the flow on this plane. We also measured the two-dimensional projection of the velocity on other horizontal planes and on the vertical plane passing through the axis of rotation and the apex of the indentation.

For each experimental run, the velocity field was extracted from the images via a cross-correlation analysis over approximately 450 oscillation periods. Depending on the experimental parameters, the final spatial resolution of the vector fields ranged between 1 vector every 1.5 or 2 mm on a square grid. For the analysis, we used an ensemble average of the velocity maps and computed the corresponding standard deviation of the two velocity components, which was found to be at most 5% of the average velocity. Note that the standard deviation averaged over the whole measurement domain was less than 1%. The differences between repetitions of experiments with identical parameters were found to be of the same accuracy as the averaged error.

The flow is governed by three dimensionless parameters: the Womersley number $\alpha = \sqrt{R_0\omega/\nu}$ (where ν is the kinematic viscosity of the fluid), the torsional oscillation

Table 1. Main parameters characterizing the experimental runs.

Experimental series	No of runs	ε (rad)	α	δ	Plane of measurement
s1	11	0.069 (3.95°)	10.7–48.0	0.3	Equatorial plane
s2	34	0.175 (10.03°)	2.5–50.4	0.3	Equatorial plane
s3	11	0.261 (14.95°)	14.5–47.7	0.3	Equatorial plane
s4	11	0.348 (19.94°)	10.7–48.0	0.3	Equatorial plane
s5	10	0.069 (3.95°)	14.5–47.7	0.2	Equatorial plane
s6	10	0.176 (10.08°)	14.5–47.7	0.2	Equatorial plane
s7	10	0.260 (14.90°)	14.5–47.7	0.2	Equatorial plane
s8	9	0.350 (20.05°)	3.5–47.6	0.2	Equaterial plane
s9	9	0.350 (20.05°)	3.5–10.6	0.1	Equatorial plane
s10	12	0.174 (9.97°)	3.5–17.6	0.3	Vertical plane
s11	12	0.174 (9.97°)	3.5–17.6	0.2	Vertical plane
s12	12	0.174 (9.97°)	3.5–17.6	0.1	Vertical plane
s13	35	0.174 (9.97°)	17.6	0.3	Horizontal planes

amplitude ε and the indentation size δ. As discussed above, δ usually lies between 0.1 and 0.3 and its value varies as the lens changes shape during focusing. During typical eye movements, ε can take any value up to $\pi/4$, whereas the value of α may take a wide range of values spanning many orders of magnitude from order 1 up to around 10^4 (Dyson *et al* 2004). The parameter values and planes of measurement used in our experiments are shown in table 1. Note that, due to limitations of our experimental apparatus, in the present study we consider values of α approximately ranging between 2 and 50. These values are representative of a fairly wide range of medically relevant conditions. In particular, small values of the Womersley number are encountered either when the vitreous cavity contains a highly viscous fluid (e.g. a tamponande fluid) or when low frequency eye movements are considered.

In order to ensure similitude between the model and the prototype scale, we need to preserve the dimensionless parameters α, ε and δ. We define the length magnification ratio as $\lambda_L = L_P/L_M \approx 0.27$ and the kinematic viscosity ratio as $\lambda_\nu = \nu_P/\nu_M$, which varies from experiment to experiment (where the subscript P denotes the prototype real eye and M the model). Imposing $\alpha_P = \alpha_M$ yields the following scale factor for the oscillation frequency: $\lambda_\omega = \omega_P/\omega_M = \lambda_\nu/\lambda_L^2$. This, in turn, implies that the velocity scale is given by $\lambda_U = U_P/U_M = \lambda_\nu/\lambda_L$. To estimate the relative strength of advective and diffusive processes for a drug in the vitreous humour, we calculate the Péclet number, $Pe = U_P L_P/D = \lambda_\nu U_M L_M/D$, where D is the drug diffusion coefficient in vitreous humour.

2.2. Post-processing of results

Fluid mixing is driven by both molecular diffusion and advection. In this paper, we consider stirring, which is the component of mixing that arises due to advection only. For steady flows, the Okubo–Weiss parameter λ_0 describes the stirring by relating it to the local flow topology and it quantifies the local rate of separation of initially close trajectories (Weiss 1981). It is defined as $\lambda_0 = -\det(\mathbf{M})$, where the tensor $\mathbf{M}$ is the gradient of the Eulerian velocity. In regions where $\lambda_0 > 0$, the flow is locally hyperbolic, strain overcomes rotation and dispersion is locally efficient. In regions where $\lambda_0 < 0$, the flow is dominated by rotation, is classified

as elliptical, and particle trapping can occur due to coherent vortical structures (Provenzale 1999, Hua and Klein 1998).

To analyse the stirring properties in more detail, we used Lagrangian quantities. We calculated particle trajectories on the equatorial plane, which is a material plane due to symmetry, determined from integrating the measured velocity fields using a fourth-order Runge–Kutta algorithm with adaptive step size, which has errors of order $(\Delta t)^4$, where Δt is the integration time step. For each flow field, we computed approximately 10^4 trajectories, seeding the flow on a regular grid with a spacing equal to half of the PIV grid and interpolating the experimental velocity vectors using a bi-cubic algorithm. Note that, since we consider a steady flow, the particle trajectories coincide with the streamlines and thus, any intersection of trajectories would be due to numerical errors in the calculation. Close inspection of the trajectories shows that the computed paths do not cross.

Once the particle trajectories are known, the absolute dispersion tensor, $\mathbf{A}^{(2)}$, can be found (see for example Provenzale (1999)):

$$A_{ij}^{(2)}(t, t_0) = \frac{1}{M} \sum_{m=1}^{M} \left\{ \left[x_i^m(t) - x_i^m(t_0) \right] \left[x_j^m(t) - x_j^m(t_0) \right] \right\}, \tag{1}$$

where M is the total number of particles, $x^m(t)$ is the position of the mth particle at time t and $x^m(t_0)$ is its initial position (at time t_0). If the flow is isotropic, $\mathbf{A}^{(2)}$ will be a multiple of the identity matrix. The mean square displacement is given by the trace of $\mathbf{A}^{(2)}$, defined as total absolute dispersion, and here we consider its dimensionless equivalent:

$$a^2 = \frac{\text{tr}(\mathbf{A}^{(2)})}{R_0^2}. \tag{2}$$

The absolute diffusivity is given by

$$K = \frac{1}{2} \frac{\mathrm{d}}{\mathrm{d}t} [\text{tr}(\mathbf{A}^{(2)})], \tag{3}$$

which has the same dimensions as the molecular diffusion coefficient D, and measures the average rate of spreading of the particles in the domain.

To study how dispersion processes are influenced by flow structures for inhomogeneous flows, we calculated the nondimensional absolute square displacement of a particle:

$$b^2(\mathbf{x}_0, t) = \frac{\|\mathbf{x}(t) - \mathbf{x}_0\|^2}{R_0^2}, \tag{4}$$

where $\mathbf{x}(t)$ is particle position at time t that satisfies $\mathbf{x}(t_0) = \mathbf{x}_0$. Note that a^2 is the spatial average of b^2.

3. Results

3.1. Description of flows

In this section, we describe the flows we observed and we will discuss the stirring that they induce in section 4. We observed a steady streaming flow for all parameter values considered, the qualitative nature of which depends strongly upon the value of α and moderately upon ε and δ, whereas its intensity depends on all three parameters. As the Womersley number is progressively increased, a sequence of topological changes occurs in the velocity field, which are described in the following paragraphs.

In figure 2, we present velocity fields on the equatorial plane for values of the Womersley number ranging from 3.8 to 45.7, keeping the oscillation amplitude and indentation size fixed ($\varepsilon = 0.17$ rad and $\delta = 0.3$). The shading shows the value of the Okubo–Weiss parameter λ_0. This helps to identify circulation structures and to distinguish regions of the flow. Large positive values of λ_0 indicate regions that are locally characterized by high levels of stirring, and low values of λ_0 show low levels of stirring. Figure 2(a) shows the flow with $\alpha = 3.8$; the anterior part of the chamber (top) is dominated by the presence of two intense circulation structures whose centres are marked by solid white circles, which we refer to as A-vortices. They are reflections of one another in the line of symmetry, and their sense of rotation is such that the flow is directed from the apex of the indentation towards the centre. Two further weak vortices are also apparent (labelled as B-vortices, solid black circles in the figure) between the previous vortices and the wall, which rotate in the opposite sense to the A-vortices. Close to the indentation, an intense hyperbolic region is clearly visible, the centre of which is marked by a white square. In the posterior part of the chamber, the flow is predominantly in the radial direction, from the wall towards the centre, and it is similar to that obtained in a perfect sphere for the same parameter values (Repetto *et al* 2008). This steady streaming pattern is in very good qualitative agreement with the analytical predictions of Repetto *et al* (2009), which are based on the assumptions of small amplitude eye rotations and small departure of the domain from the spherical shape (small ε and δ) and small to moderate values of α. As α increases, figures 2(b) and (c), the A-vortices decrease in size and move towards the indentation, and the B-vortices grow in size and intensity. A further increase in α produces two new vortical structures, C-vortices, the centres of which are marked by open circles, figure 2(d). The C-vortices have the opposite sense of rotation from the A-vortices, which are squeezed between the C-vortices and the indentation. The flow between these vortices is now directed from the centre towards the indentation.

For the largest values of α considered (figures 2(e) and (f)), the C-vortices become dominant, both in size and intensity. The flow in the posterior region is not significantly affected by the presence of the lens.

We obtained a qualitatively similar sequence of flows for all values of ε and δ tested. However, a decrease in either ε or δ increases the value of α for which both the B- and C-vortices first appear.

The measurements shown in figure 2 are relative to the equatorial plane, which is a plane of symmetry for the flow under investigation. The vortices described, however, are a slice of a more complicated three-dimensional flow structure. To get some insight into the three dimensionality of the flow, experiments have been carried out to measure the 2D velocity fields on horizontal planes (orthogonal to the axis of rotation) at different heights, from the equatorial plane towards the north pole of the eye model, and also on the plane containing the apex of the indentation and the axis of rotation.

Horizontal projections of the velocity vectors measured on different horizontal planes (series s13) are shown in figure 3. As z increases, the A-vortices become closer to each other, remaining visible up to approximately $z = 0.625R_0$, figure 3(c), which is approximately the maximum extent of the indentation. This suggests that the A-vortices take the form of a three-dimensional toroidal structure around the edge of the indentation, which is corroborated by measurements on the vertical plane.

Two examples of velocity fields in the vertical plane (from series s4) are shown in figure 4. In the anterior (right-hand side), the velocity is larger due to the indentation. Two intense vortical structures, one in each hemisphere, are visible, whose sense of rotation is consistent with the flows shown in figures 2(a) and (b), which have similar parameter values. In the posterior of the domain, the indentation has little effect on the flow.
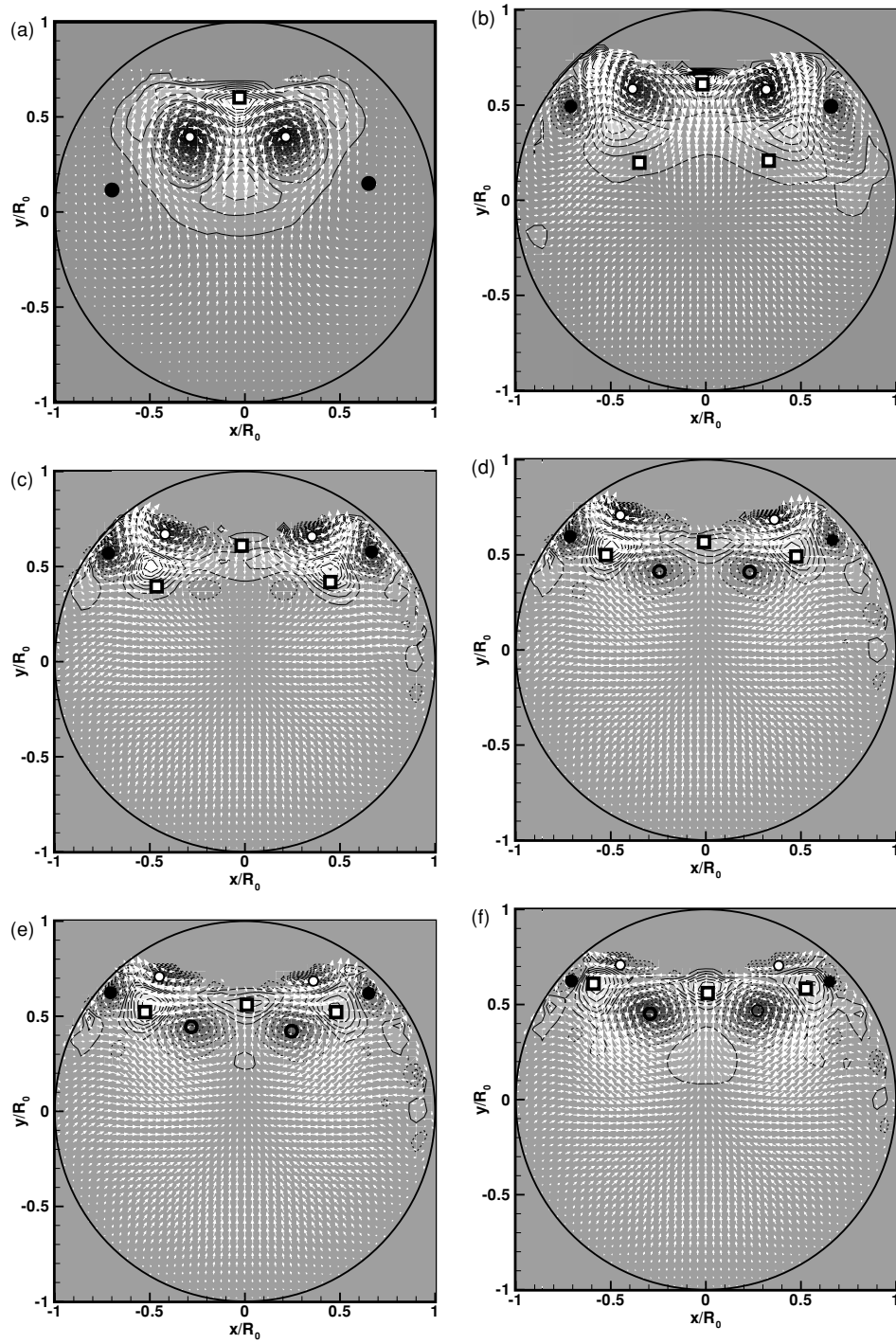
Figure 2. Flow vectors and contours of λ_0 (shaded) for experiments in series s2 ($\delta = 0.3$, $\varepsilon = 0.17$ rad): (a) $\alpha = 3.8$; (b) $\alpha = 16.9$; (c) $\alpha = 27.6$; (d) $\alpha = 33.8$; (e) $\alpha = 36.5$; (f) $\alpha = 45.7$. Circles mark the centres of vortices: solid white circles: A-vortices; solid black circles: B-vortices; open circles: C-vortices. Solid white squares mark the centres of the hyperbolic regions.
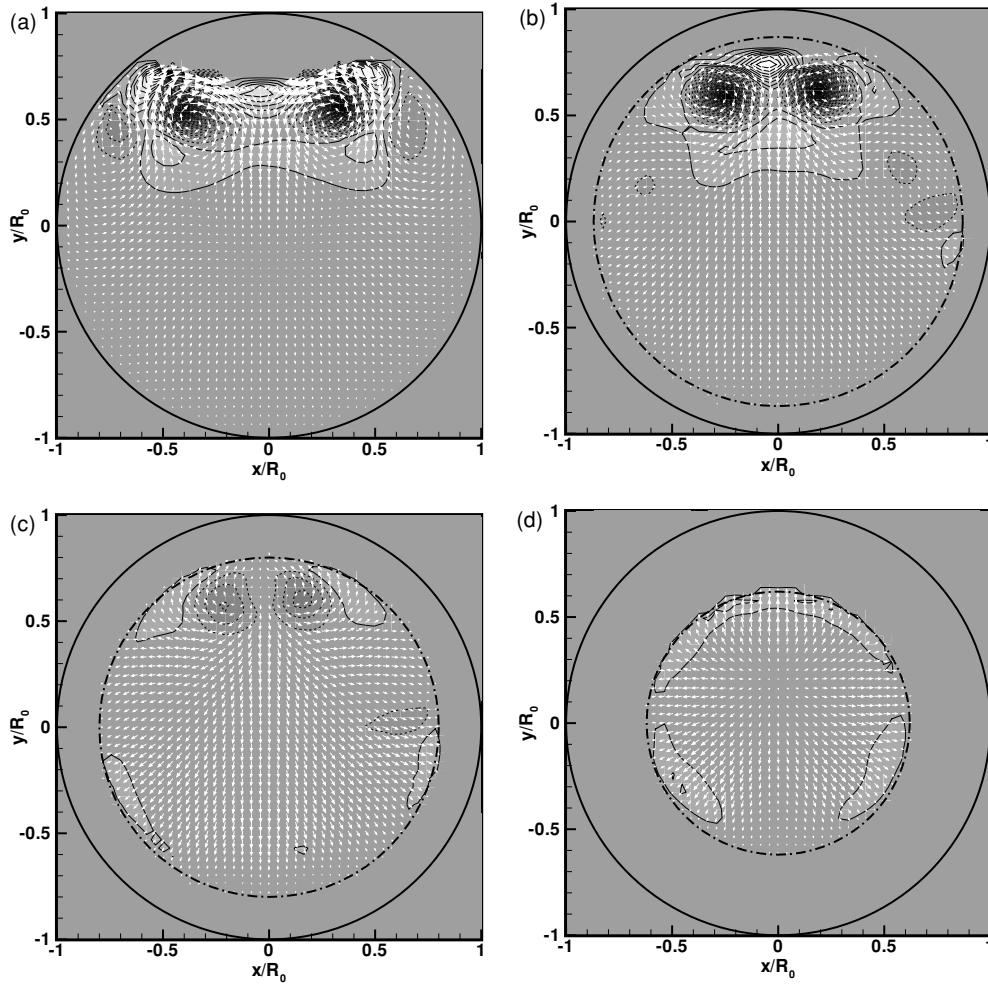
Figure 3. Horizontal velocity components and contours of λ_0 (shaded) on horizontal planes (series s13, $\varepsilon = 0.174$, $\alpha = 17.6$) at different heights: (a) $z/R_0 = 0$; (b) $z/R_0 = 0.5$; (c) $z/R_0 = 0.625$; (d) $z/R_0 = 0.75$. The circle drawn with a solid line indicates the size of the equatorial plane, whereas the circle with a dashed-dot line indicates the actual dimension of the domain at different values of z/R_0.

3.2. Analysis of the flows

We define a synthetic measure of the intensity of the steady streaming and investigate its dependence on the parameters. One possible measure is the maximum streaming velocity, which was used in Repetto *et al* (2008) for flow in a rotating sphere. However, this measure is delicate, since it is based on a measurement at a single point, so here we use a more robust quantity: the spatial average of the magnitude of the streaming velocity over the equatorial plane, denoted by U. Graphs of the dimensionless quantity $I = U/\omega R_0$, which we refer to as the 'intensity', are shown in figure 5. It is plotted as a function of α in figure 5(a) for three values of ε and for $\delta = 0.2$. For $\varepsilon = 0.34$ rad (squares) and small α, I grows rapidly with α until it reaches a local maximum. As α increases further, the intensity decreases, attaining a local
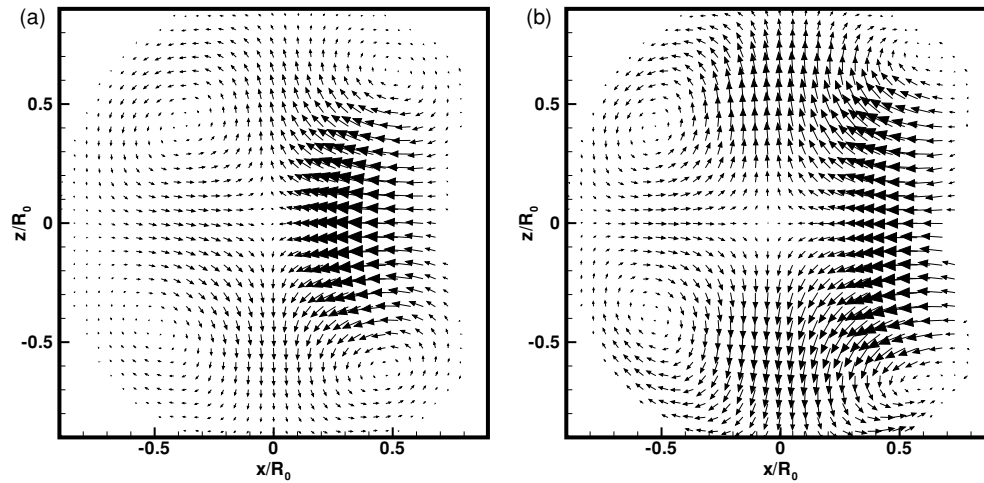
**Figure 4.** Velocity vectors onto the vertical plane containing the axis of rotation and the apex of the indentation (series s10, $\delta = 0.3$, $\varepsilon = 0.17$ rad). (a) $\alpha = 3.5$; (b) $\alpha = 17.6$.
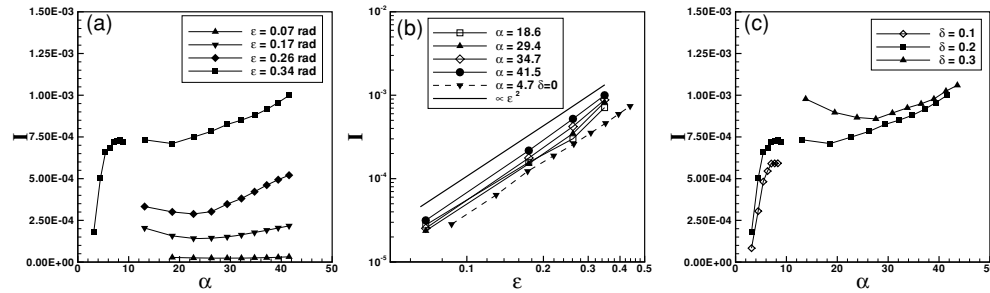
Figure 5. Plots of the steady streaming intensity (dimensionless averaged velocity): (a) as a function of α for $\delta = 0.2$ and different values of ε; (b) as a function of ε for $\delta = 0.2$ and different values of α, the results for the case $\delta = 0$ (Repetto *et al* 2008) are also reported, note that the plot has logarithmic axes; (c) as a function of α for $\varepsilon = 0.35$ rad and different values of δ.

minimum approximately in correspondence with the appearance of the C-vortices ($\alpha \approx 20$), figures 2(c) and (d). In the case of a spherical domain, the intensity tends asymptotically to a constant value, see figure 4(a) of Repetto *et al* (2008). Here the intensity is dominated by the presence of the hyperbolic region, which is not present in the spherical case, so there is no reason necessarily to expect similar behaviour, although we cannot rule out the possibility of an asymptotic value of *I* at higher α. For different values of ε, the curve is qualitatively similar. The local minimum is still present, but, as ε decreases it occurs at larger values of α, approximately corresponding to the value of α at the formation of the C-vortices.

The relationship between *I* and ε is plotted in figure 5(b), and this shows a close match to a power law dependence with exponent 2, which agrees with the predictions of Repetto *et al* (2008) for the spherical case and of Repetto *et al* (2008) for the weakly deformed sphere. The results of Repetto *et al* (2008) for $\delta = 0$ are also shown in the figure. In figure 5(c), there is only a partial overlap in the range of α between the different experimental series; however, the graphs suggest that, as expected, *I* increases as δ increases, and that this effect becomes smaller for very large α.
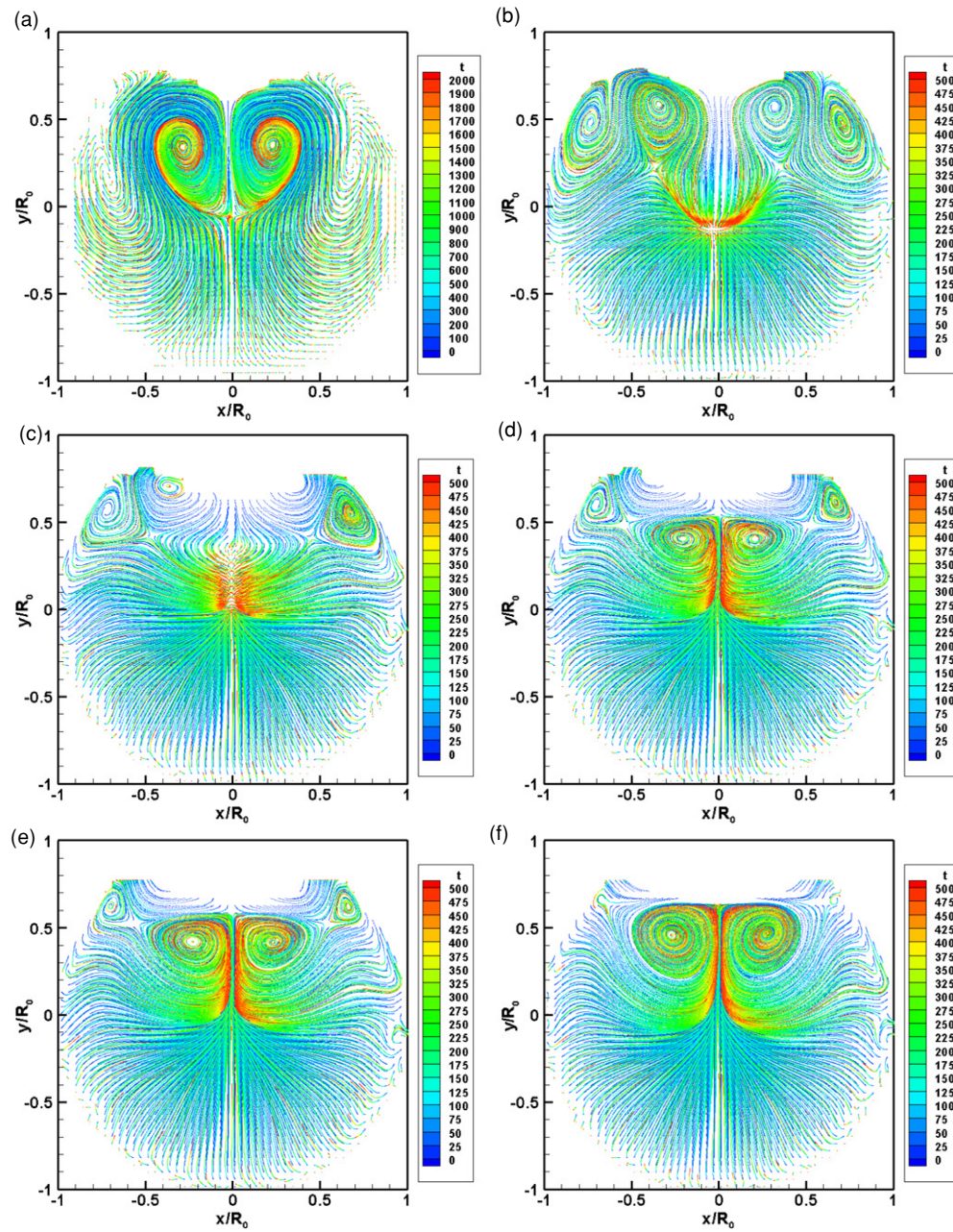
Figure 6. Particle trajectories corresponding to velocity fields shown in figure 2. Series s2 ($\delta = 0.3$, $\varepsilon = 0.17$ rad): (a) $\alpha = 3.8$; (b) $\alpha = 16.9$; (c) $\alpha = 27.6$; (d) $\alpha = 33.8$; (e) $\alpha = 36.5$; (f) $\alpha = 45.7$.

4. Stirring processes

In figure 6, we report the particle trajectories corresponding to the Eulerian velocity fields shown in figure 2. The colour indicates the integration time (blue is the start and red the
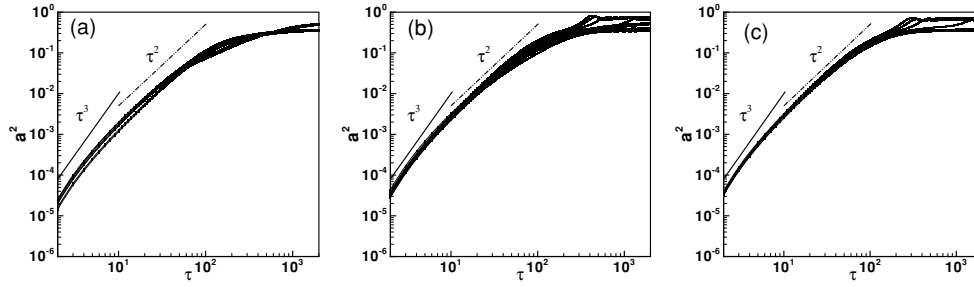
Figure 7. Nondimensional absolute dispersion a^2 against nondimensional time τ for $\epsilon = 0.35$ rad: (a) $\delta = 0.1$ (series s9); (b) $\delta = 0.2$ (series s8); (c) $\delta = 0.3$ (series s4). Each line corresponds to a different value of α. Note that all plots have log–log scales.

end of the trajectory). The elliptic and hyperbolic regions are clearly visible, and these undergo topological changes agreeing with those described in section 3. As particles approach hyperbolic points, they are rapidly swept away. On the other hand, near elliptical points the trajectories are confined to spiral paths around them and the velocity is low.

We also used the particle trajectories to calculate the nondimensional total absolute dispersion a^2 and the absolute diffusivity K. For short times, a^2 is expected to depend strongly on the topological characteristics of the flow, whereas for sufficiently large times the average particle path has a length comparable to the size of the domain, and for a perfectly mixing flow a^2 will tend to the dimensionless mean square distance between two points placed at random in a unit circle, which is given by

$$\frac{2}{\pi} \int_0^1 \int_0^1 \int_0^{2\pi} \sqrt{(r_1 \cos(\theta) - r_2)^2 + r_1^2 \sin(\theta)^2} \, r_1 r_2 \, \mathrm{d}\theta \, \mathrm{d}r_1 \, \mathrm{d}r_2 \approx 0.905. \quad (5)$$

Figure 7 shows the evolution in dimensionless time ($\tau = t/T$) of the nondimensional absolute dispersion for various values of α and δ. In each case, when τ is of order at most 10^2, a^2 and τ obey an approximate power law relationship with exponent between 2 and 3, which is similar to the results of Rossi *et al* (2006), who also considered, albeit in a different context, multi-scale laminar flows. They also obtained flows with elliptic and hyperbolic points and found that a^2 grows faster than t^2. In fact, the exponent of the power law mainly depends on the existence and persistency of the stagnation points and it has a weak dependence on α, ε and δ.

For long times, a^2 tends approximately to a constant value, which is expected in a closed domain, and the limiting value ranges between 0.7 and 1.1. Both the value itself and the time required to attain it are strongly dependent on the amplitude of the oscillation ε and the indentation size δ. We used the results to compute the absolute diffusivity coefficient K, which measures the rate of spreading of a cloud of particles, and found values ranging on the order of 10^{-4} to 10^{-1} m^2 s^{-1}. For Brownian dispersion in an unbounded domain, K has a constant value (Rossi *et al* 2006) whereas in our case K rises to a maximum before falling back to zero for large τ, when a^2 attains an almost constant value.

When the flow is inhomogeneous, as in the present case, it is of some interest to study how the dispersion processes are locally influenced by the flow structures. This cannot be captured by a^2, which is an average over the domain, so instead we plot the spatial distribution of the square displacement, b^2, which can reveal regions of particle trapping (low values) and efficient stirring (high values). In figure 8, we show plots of b^2 for the same flows as shown in figures 2(a) and (f), each at three different times. These show that the distance travelled
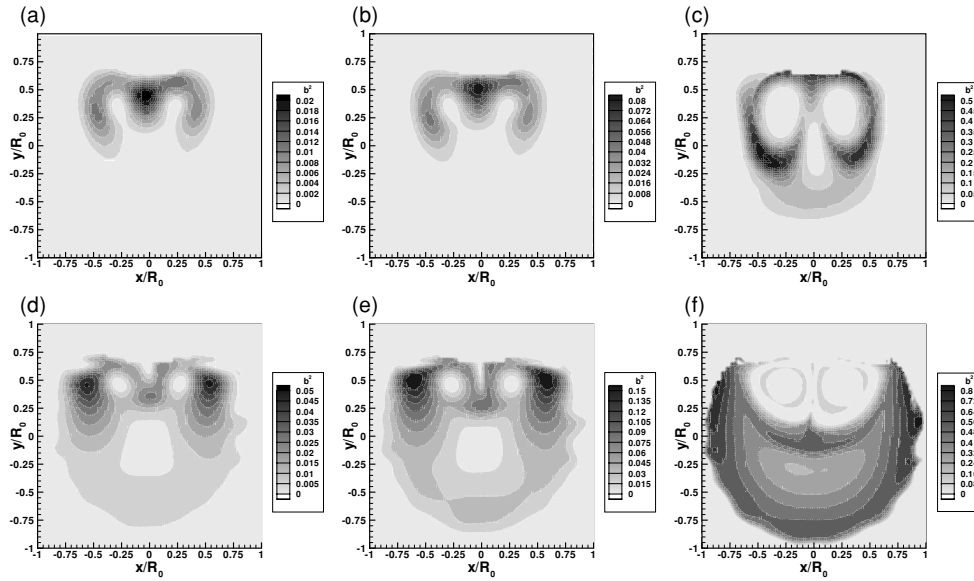
Figure 8. Contour plots of the nondimensional absolute square particle displacement b^2, defined by equation (4), for two experiments of series s2. All plots are for $\delta = 0.3$, $\varepsilon = 0.17$ rad. In (a, b, c), $\alpha = 3.8$; in (d, e, f), $\alpha = 45.7$. (a, d) $\tau = 50$; (b, e) $\tau = 100$; (c, f) $\tau = 500$.

by a particle depends strongly on its initial location. Dark regions indicate efficient stirring, which coincide with neighbourhoods of the hyperbolic points, while lighter colours indicate low stirring, which correspond to elliptic points (vortical structures). The closed circulations act as mass trapping structures, particularly the A-vortices for low α and the C-vortices for high α.

5. Conclusions

An improved understanding of mixing processes in the vitreous chamber due to fluid motion is important to ensure effective delivery of drugs intended for the retina. In this work, we used a model of the vitreous chamber of the eye to study the fluid motion and mixing induced by idealized sinusoidal torsional oscillations of the eyeball. We concentrated on the effect of the shape of the posterior chamber, specifically the indentation in the anterior part due to the lens. We considered a Newtonian fluid, which is relevant when either the vitreous is liquefied or it has been replaced, after vitrectomy, by a purely viscous tamponade fluid. Moreover, this work is a necessary step towards investigating fluids with more complex rheological behaviour. The flow is governed by three dimensionless parameters: the Womersley number α, the oscillation amplitude ε and the indentation size δ. Using physiologically relevant parameter values, we calculated the steady streaming component of the flow, which, as pointed out by Repetto *et al* (2009), has a much larger effect on mixing in the domain than the oscillatory component.

In this paper, we considered stirring processes, neglecting the effect of diffusion. In order to ascertain the relative importance of advection and diffusion we now calculate an *a posteriori* estimate of the Péclet number of the flow. In section 2, we showed that the Péclet number of the flow in the vitreous chamber (prototype scale) is $Pe = \lambda_\nu U_M L_M / D$, where λ_ν is the ratio of kinematic viscosities between prototype and model, U_M and L_M are typical velocity and length

scales, respectively, and D is the diffusion coefficient. We take U_M to be the spatial average of the magnitude of our streaming velocity over the equatorial plane, $L_M = R_0 = 0.0408$ m (radius of the sphere) and $D \approx 6 \times 10^{-10}$ m^2 s^{-1} (diffusion coefficient of fluorescein, a commonly used diagnostic tool, in the vitreous humour (Kaiser and Maurice 1964)). The calculated Péclet numbers range from approximately 10^3 (at low values of α, ε and δ) up to a maximum of approximately 10^6, which is consistent with the theoretical predictions obtained in Repetto *et al* (2009), valid for small ε and δ and moderate values of α. Hence the estimated Péclet number is very large in all cases, suggesting that advective processes play a crucial role in inducing mass transport in the vitreous chamber and largely overcome diffusive processes in the case of liquefied vitreous humour.

We may also use the measurement of the absolute diffusivity coefficient to evaluate the time required for a particle to travel a distance of one radius; this is given by $R_0^2/K \approx 1$–100 s depending on the value of K. On comparing this with the diffusive timescale, $R_0^2/D \approx$ 2.7 days, it can immediately be seen that advection is several orders of magnitude more efficient in inducing mass transport. Note that, according to Atluri and Mitra (2003), the residence time of chemicals injected into the vitreous humour in rabbit eyes is of order of hours, i.e. much larger than the time required for a fluid particle to travel a distance of one radius, at least in the case considered here of purely viscous fluid.

Our experiments reveal complex structures in the flow. On the equatorial plane, elliptic and hyperbolic regions organize the mass transport. Particle trapping occurs in elliptic regions, corresponding to low stirring, while conversely hyperbolic regions are responsible for high stirring. Moreover, for larger Womersley number, a complex sequence of topological changes takes place in the flow, giving rise to particle paths that lead directly from the posterior to the anterior of the chamber. At low frequencies, particles from both the anterior and the posterior tend to drift towards the centre of the eye. Hence we predict significantly faster mass transport from the posterior to the anterior of the eye for high-frequency oscillations than for low-frequency oscillations.

The intensity of the streaming flow increases as the oscillation frequency increases, but has a local minimum due to a topological change in the flow (creation of new vortices). Its dependence on ε closely follows a power law and it also increases with increasing δ. For small times, the absolute dispersion increases faster than the square of the time, which is due to the presence of hyperbolic stagnation points in the flow.

References

Atluri H and Mitra A K 2003 Disposition of short-chain aliphatic alcohols in rabbit vitreous by ocular microdialysis *Exp. Eye Res.* **76** 315–20

Balachandran R and Barocas V 2008 Computer modeling of drug delivery to the posterior eye: effect of active transport and loss to choroidal blood flow *Pharm. Res.* **25** 2685–96

Balachandran R K, Kevin D, Dorfman K D and Barocas V H 2008 Dispersion of the drug in the liquid vitreous due to saccadic eye movements *Proc. ASME 2008 Summer Bioengineering Conf. (SBC2008) (Marco Island, FL, 25–29 June)*

Cunha-Vaz J G 2004 The blood–retinal barriers system. Basic concepts and clinical evaluation *Exp. Eye Res.* **78** 715–21

David T, Smye S, Dabbs T and James T 1998 A model for the fluid motion of vitreous humour of the human eye during saccadic movement *Phys. Med. Biol.* **43** 1385–99

Dyson R, Fitt A J, Jensen O E, Mottram N, Miroshnychenko D, Naire S, Ocone R, Siggers J H and Smithbecker A 2004 Post re-attachment retinal re-detachment *Proc. 4th Medical Study Group* University of Strathclyde, Glasgow

Ethier C R, Johnson M and Ruberti J 2004 Ocular biomechanics and biotransport *Ann. Rev. Biomed. Eng* **6** 249–73

Hua B L and Klein P 1998 An exact criterion for the stirring properties of nearly two-dimensional turbulence *Physica D* **113** 98–110

Kaiser R J and Maurice D M 1964 The diffusion of fluorescein in the lens *Exp. Eye Res.* **3** 156–65

Kathawate J and Acharya S 2008 Computational modeling of intravitreal drug delivery in the vitreous chamber with different vitreous substitutes *Int. J. Heat Mass Transfer* **51** 5598–609

Lee B, Litt M and Buchsbaum G 1992 Rheology of the vitreous body. Part I: viscoelasticity of human vitreous *Biorheology* **29** 521–33

Provenzale A 1999 Transport by coherent barotropic vortices *Ann. Rev. Fluid Mech.* **31** 55–93

Repetto R, Siggers J H and Stocchino A 2008 Steady streaming within a periodically rotating sphere *J. Fluid Mech.* **608** 71–80

Repetto R, Siggers J and Stocchino A 2009 Mathematical model of flow in the vitreous humor induced by saccadic eye rotations: effect of geometry *Biomech. Model. Mechanobiol.* doi:10.1007/s10237-009-0159-0

Repetto R, Stocchino A and Cafferata C 2005 Experimental investigation of vitreous humour motion within a human eye model *Phys. Med. Biol.* **50** 4729–43

Rossi L, Vassilicos J C and Hardalupas Y 2006 Multiscale laminar flows with turbulentlike properties *Phys. Rev. Lett.* **97** 144501

Stocchino A, Repetto R and Cafferata C 2007 Eye rotation induced dynamics of a Newtonian fluid within the vitreous cavity: the effect of the chamber shape. *Phys. Med. Biol.* **52** 2021–34

Weiss J 1981 *The Dynamics of Enstrophy Transfer in Two-Dimensional Hydrodynamics* (La Jolla, CA: Center for Studies of Nonlinear Dynamics, La Jolla Institute)

Xu J, Heys J J and Barocas V H 2000 Permeability and diffusion in vitreous humor: implications for drug delivery *Pharm. Res.* **17** 664–9

Yasukawa T, Ogura Y, Tabata Y, Kimura H, Wiedemann P and Honda Y 2004 Drug delivery systems for vitreoretinal diseases *Prog. Retin. Eye Res.* **23** 253–81